On the Use of Tomographically Derived Reflectivity Profiles for Pol-InSAR Forest Height Inversion in the Context of the BIOMASS Mission

Roman Guliaev, Jun Su Kim, Matteo Pardini and Konstantinos P. Papathanassiou, *Fellow, IEEE*

***Abstract* — Model-based forest height inversion from single- and multi-baseline Pol-InSAR data is today well-established. One of the critical performance points is the parameterisation of the vertical reflectivity profile. In this paper, the parameterisation of the vertical reflectivity profile using a tomographic reconstruction is proposed. To mitigate the limitations in the tomographic reconstruction induced by the limited vertical resolution especially for the ground scattering component, the ground and volume contributions are separated using the Sum of Kronecker Products (SKP) decomposition. For the forest height inversion, the Pol-InSAR line inclination angle is proposed, which, unlike the absolute coherence and the phase center, is invariant to the presence of a residual Dirac-like ground scattering contribution. The inversion performance is addressed and compared for both single- and multi-baseline cases, in the absence and presence of temporal decorrelation. In all cases the ground elevation is estimated from the tomographically reconstructed vertical reflectivity profiles and its accuracy directly influences the achieved inversion performance. The proposed methodology establishes a link between interferometric and tomographic measurements and is therefore relevant for missions that allow the implementation of both techniques. ESA's BIOMASS is one such mission, and as such is being used as a test case to discuss different implementation scenarios. The different inversion strategies are applied on P-band campaign data acquired in the frame of the AFRISAR 2016 experiment and validated against reference measurements.**

***Index Terms*—Forest Height Estimation, Synthetic Aperture Radar (SAR), Polarimetric SAR Interferometry (Pol-InSAR), SAR Tomography (TomoSAR).**

I. INTRODUCTION

ACCURATE forest height estimates at sub-hectare scales derived from remote sensing data are critical as they support the characterisation of the forest successional state and/or its disturbance regime. At the same time forest height even at lower spatial resolution can be used to initialise (or constrain) model estimates of above ground biomass and associated carbon flux components [1] [2] [3] [4].

Forest height estimation by means of model-based Polarimetric Interferometric Synthetic Aperture Radar (Pol-InSAR) measurements inversion is an established approach for getting forest height by exploring the inherent sensitivity of interferometric measurements to the vertical distribution of scatterers (also known as vertical reflectivity profile). The performance strengths and limitations of this approach are well understood, demonstrated and validated at different frequencies, from X- down to P-band, for a variety of forest and terrain conditions [5] [6] [7] [8] [9] [10].

One of the critical points in the model-based Pol-InSAR data inversion is the definition of the inversion model, especially the parameterisation of the vertical reflectivity profile. The number of parameters required to parameterise the vertical reflectivity profile has to be balanced with the number of measurements available. As the total number of measurements is limited, only very generic forms of forest vertical reflectivity profiles become applicable. [11] [12] [13] [14] [15].

In recent years, the dynamic development of SAR tomography in recent years, that allows the reconstruction of the 3D distribution of scatterers, triggered the integration of tomographic SAR measurements as a complement to conventional interferometric SAR measurements in a number of planned space-borne SAR missions [16] [17]. ESA's BIOMASS mission is such an example: a tomographic phase in the first year of operations (where 7 polarimetric acquisitions will be performed in a tomographic 3-day repeat-pass mode) will be followed by a number of interferometric cycles (each lasting about 9 months with 3 polarimetric acquisitions performed in an interferometric 3-day repeat-pass mode) for the remaining of the mission lifetime [16].

In such a scenario, where tomographic and interferometric measurements are available, the obvious question that arises is if and how the tomographically reconstructed 3D reflectivity can be used to support/improve the parameterisation of the

The authors are with the Microwave and Radar Institute, German Aerospace Center DLR Oberpfaffenhofen, 82234 Wessling, Germany (e-mail: roman.guliaev@dlr.de; junsu.kim@dlr.de; matteo.pardini@dlr.de; kostas.papathanassiou@dlr.de)

vertical reflectivity profile(s) used for the forest height inversion from the interferometric measurements. This paper aims to provide a first answer to this question. For this, Section II reviews the theoretical background and formalism of polarimetric interferometric and tomographic measurements and discusses the rationale for combining interferometric and tomographic measurements. In Section III, the forest height inversion is discussed for single and multi-baseline configurations in the absence as well as in the presence of temporal decorrelation. In the absence of temporal decorrelation and predetermined vertical reflectivity, a Pol-InSAR estimate exclusively dependent on forest height, is derived. The experimental data used for the demonstration of the proposed inversion approach(es) are described in Section IV. In Section V the achieved experimental inversion results are described and discussed while the conclusions are presented in Section VI. While the proposed approach provides a generic way to link interferometric and tomographic measurements at lower frequencies and is thus relevant for a number of missions that allow the implementation of both techniques, ESA's BIOMASS mission is used as a reference for the scenarios discussed.

II. Theoretical background

A. Interferometric measurements

Across-track SAR interferometry relies on a rather limited number (a couple of or few more) single-look complex (SLC) SAR images $s_i(\vec{w})$, acquired under slightly different look angles at a given polarisation . The three-dimensional unitary complex vector $\vec{w}$ determines the choice of polarisation as defined in [6]. The complex interferometric coherence, $\tilde{\gamma}_{Obs}(\vec{w})$ is defined as the normalised cross-correlation of the two images forming the interferogram $s_1(\vec{w})$ and $s_2(\vec{w})$ [18]:

$$\tilde{\gamma}_{Obs}(\vec{w}) = \frac{\langle s_1(\vec{w}) s_2^*(\vec{w}) \rangle}{\sqrt{\langle s_1(\vec{w}) s_1^*(\vec{w}) \rangle \langle s_2(\vec{w}) s_2^*(\vec{w}) \rangle}}, \quad (1)$$

where $\langle \dots \rangle$ denotes the statistical expectation.

The interferometric coherence can be parameterised into several independent decorrelation contributions superimposed in a multiplicative way as [12] [18] [19]:

$$\tilde{\gamma}_{Obs}(\vec{w}) = \tilde{\gamma}_{Tmp}(\vec{w}) \tilde{\gamma}_{Rg} \tilde{\gamma}_{Sys}(\vec{w}) \tilde{\gamma}_{Vol}(\vec{w}), \quad (2)$$

where $\tilde{\gamma}_{Tmp}(\vec{w})$ accounts for the temporal decorrelation, $\tilde{\gamma}_{Rg}$ the baseline induced range spectral decorrelation, while $\tilde{\gamma}_{Sys}(\vec{w})$ comprises various system induced decorrelations, including additive noise decorrelation etc.

The volumetric decorrelation $\tilde{\gamma}_{Vol}(\vec{w})$ is defined as the Fourier transform of the vertical reflectivity profile $F(z, \vec{w})$ within the reflectivity volume, i.e. from the ground to the top of the forested layer of height h_v:

$$\tilde{\gamma}_{Vol}(k_z, \vec{w}) = e^{j\varphi_0} \frac{\int_0^{h_V} F(z, \vec{w})\, e^{jk_z z} dz}{\int_0^{h_V} F(z, \vec{w})\, dz}, \quad (3)$$

where φ_0 is the ground phase related to the ground elevation z_0 by $\varphi_0 = k_z z_0$. The vertical wavenumber k_z is proportional to the look angle difference $\Delta\theta$ between the two acquisitions and inverse proportional to the incidence angle θ_0, defined in the monostatic case as

$$k_z = \frac{4\pi}{\lambda} \frac{\Delta\theta}{\sin(\theta_0)}. \quad (4)$$

After normalisation, by substituting $z' = z/h_v$, equation (3) rewrites to

$$\tilde{\gamma}_{Vol}(k_z, \vec{w}) = e^{j\varphi_0} \frac{\int_0^1 F(h_v z', \vec{w})\, e^{jk_z h_v z'} dz'}{\int_0^1 F(h_v z', \vec{w})\, dz'}. \quad (5)$$

According to (5), if the vertical reflectivity $F(h_v z', \vec{w})$ is known, forest height can be inverted, by means of a balanced inversion problem, from a single $\tilde{\gamma}_{Vol}(k_z, \vec{w})$ measurement [9] [20]. It is important to note from (5) that the forest height estimation is modulated by the unitless product $k_z h_v$ rather than by h_v or k_z alone. As a consequence, larger k_z values allow more accurate estimates of lower forest heights while smaller k_z are required for an accurate estimation of taller forest heights [4] [21].

The range spectral decorrelation $\tilde{\gamma}_{Rg}$ can be significant if the k_z approaches a critical value k_z^{crit} that is proportional to the system bandwidth W_{rg}:

$$\tilde{\gamma}_{Rg} = 1 - \frac{k_z}{k_z^{crit}} \quad (6)$$

with

$$k_z^{crit} = \frac{2\pi}{c} W_{rg} \cos(\theta_0). \quad (7)$$

Therefore, for systems with narrow system bandwidths such as BIOMASS (with $W_{rg}^{BIOMASS}$=6MHz), the range spectral decorrelation contributes significantly to the overall decorrelation level.

B. Polarimetric interferometric coherence optimisation

Quad-polarimetric SAR acquisitions provide three independent polarimetric images $s_i(\vec{w}_1), s_i(\vec{w}_2), s_i(\vec{w}_3)$ which are used to form the polarimetric data vector $\vec{y}_p^i$:

$$\vec{y}_p^i = [s_i(\vec{w}_1), s_i(\vec{w}_2), s_i(\vec{w}_3)]^T, \quad (8)$$

where $(\dots)^T$ denotes the transpose operator. The statistically averaged outer product of the two co-registered interferometric polarimetric vectors $\vec{y}_p^i$ form the polarimetric interferometric covariance matrix Ω_{12} [22]:

$$[\Omega_{12}] = \langle \vec{y}_p^{\,1} \cdot \vec{y}_p^{\,2\,H} \rangle \tag{9}$$

as well as the polarimetric covariance matrices:

$$[T_{11}] = \langle \vec{y}_p^{\,1} \cdot \vec{y}_p^{\,1\,H} \rangle \text{ and } [T_{22}] = \langle \vec{y}_p^{\,2} \cdot \vec{y}_p^{\,2\,H} \rangle, \tag{10}$$

where $(\dots)^H$ denotes the Hermitian operator. The mean coherency matrix [T]:

$$[T] = \frac{[T_{11}] + [T_{22}]}{2} \tag{11}$$

can be used to obtain a normalised form of the polarimetric interferometric covariance matrix:

$$[\Pi_{12}] = [T]^{-\frac{1}{2}} [\Omega_{12}] [T]^{-\frac{1}{2}}. \tag{12}$$

The normalised form of covariance matrix is used for the calculation of the coherence region, i.e. the locus of points on the complex plane which represents Pol-InSAR coherences by varying the projection vector $\vec{w}$ [22] [23], and the trace coherence [24] defined in Chapter III.

C. Tomographic measurements

SAR tomography relies on a set of single-look complex (SLC) SAR images $s_1(\vec{w}), s_2(\vec{w}), \dots, s_M(\vec{w})$ acquired along spatially (and temporal) displaced tracks. The set of the M co-registered and (phase) calibrated SLC images forms the so-called tomographic (data) stack and can be written in form of a (column) data vector $\vec{y}$ as:

$$\vec{y}(\vec{w}) = [s_1(\vec{w}), s_2(\vec{w}), \dots, s_M(\vec{w})]^T. \tag{13}$$

The full information of the tomographic stack can be represented by its $(M \times M)$-dimensional covariance matrix:

$$[R] = \langle \vec{y}(\vec{w}) \cdot \vec{y}^{\,H}(\vec{w}) \rangle \tag{14}$$

with $R_{mn} = \langle s_m(\vec{w})\, s_n^*(\vec{w}) \rangle$. Each element R_{mn} of [R] corresponds to an image pair formed by the m-th and n-th image of the stack and can be related to the vertical reflectivity profile via a Fourier relation:

$$R_{mn} = \int F(z, \vec{w})\, e^{j k_z^{mn} z}\, dz, \tag{15}$$

where k_z^{mn} is the vertical wavenumber associated to the pair formed by the m-th and the n-th images of the stack:

$$k_z^{mn} = 2\frac{2\pi}{\lambda}\frac{\Delta\theta^{mn}}{\sin(\theta_0)}. \tag{16}$$

A regular orbit progression results in a uniform distribution of vertical wavenumbers.

Equation (15) states that the covariance associated to each image pair of the tomographic stack represents one spectral sample of $F(z, \vec{w})$ in the vertical wavenumber domain. The whole set of spectral samples provided by the tomographic stack is represented by its covariance matrix [R]. In this sense, the tomographic reconstruction can be addressed as a spectral estimation problem [25].

The integral in (15) can be discretised in a set of H heights $\{z_i\}_{i=1}^{H}$ and rewritten as

$$\vec{r}(\vec{w}) = [A]\vec{f}(\vec{w}) \tag{17}$$

where $\vec{r}(\vec{w}) = \mathrm{vec}([R])$ is the vector representation of [R], i.e. an M^2-dimensional column vector obtained by stacking the columns of [R], each one on top of the other, and $\vec{f}(\vec{w})$ is a H-dimensional column vector with generic elements $[f]_i = F(z_i, \vec{w})$. [A] is a $(M^2 \times H)$-dimensional matrix defined as [26]:

$$[A] = [e^{j\mathrm{vec}([K])z_1} \quad \dots \quad e^{j\mathrm{vec}([K])z_H}]. \tag{18}$$

Each column of [A] is obtained from the vectorisation of the $(M \times M)$-dimensional matrix [K] with generic element $[K]_{mn} = k_z^{mn}$. Estimates of $F(z_i, \vec{w})$ are obtained by solving the system of $M(M-1)/2$ equations with H unknowns.

Since volume scatterers are characterised by extended and continuous vertical reflectivity profiles, the number of usually available images M is generally not sufficient to obtain the required sampling H in the inversion problem. One approach to deal with this is to estimate $F(z_i, \vec{w})$ as the output power of a filter (referred in the following as the vertical power profile $P(z_i, \vec{w})$), whose response is defined by a (height-varying) M-dimensional set of coefficients $\vec{h}(z_i)$. In this case, $P(z_i, \vec{w}) = \langle |h^H(z_i)\vec{y}(\vec{w})|^2 \rangle$ is obtained in the form [25]:

$$P(z_i, \vec{w}) = \vec{h}(z_i)^H [R] \vec{h}(z_i). \tag{19}$$

The generic $\vec{h}(z_i)$ is designed to allow only the backscatter contribution at z_i to pass, while cancelling out the contributions at the other heights. However, the often small M prevents a complete cancellation. Thus, the choice of $\vec{h}(z_i)$ affects the final vertical resolution and the contrast (i.e. the sidelobe level) of the reconstructed $P(z_i, \vec{w})$. Fourier and Capon beamformers are such filter-based reconstruction algorithms [25] [27].

The Fourier algorithm reconstructs the underlying 3D reflectivity in form of its convolution with the vertical Point Spread Function (PSF) that makes the quality and the vertical resolution of the reconstructed profile strongly dependent on the number and distribution of the available vertical wavenumbers. Accordingly, two parameters characterise the tomographic reconstruction. The first one is the vertical Rayleigh resolution δ_z that is inversely proportional to the largest vertical wavenumber $k_{z,max} = \max\{k_z^{mn}\}$ [26] [27]:

$$\delta_z = \frac{2\pi}{k_{z,max}}. \tag{20}$$

The finite sampling in the wavenumber domain causes the appearance of replicas of $F(z, \vec{w})$ in any of its reconstructions. The width of the non-ambiguous tomographic reconstruction height interval is given (for a uniform distribution of vertical wavenumbers) by [26] [27]:

$$h_{amb} = \frac{2\pi}{k_{z,min}}, \quad (21)$$

where $k_{z,min} = \min\{k_z^{mn}\}$.

Since the tomographically reconstructed vertical power profiles $P(z_i, \vec{w})$ represent a convolved form of the underlying power profile, their direct use to substitute the vertical reflectivity profile $F(z, \vec{w})$ in (5) might be problematic. The limited vertical resolution of the reconstructed vertical power profile is insufficient to accurately represent isolated Dirac-like scattering contributions (as induced by the ground) that become stretched, i.e. smeared out. In the following, an attempt to separate the ground contribution from the tomographically reconstructed profiles is discussed in order to allow an alternative forest height inversion modeling approach.

D. Polarimetric tomography and ground-volume separation

The polarimetric tomographic stack consists of 3M SLC images that can be written in form of a 3M dimensional (column) data vector $\vec{y}$ as:

$$\vec{y}_p = [s_1(\vec{w}_1), s_1(\vec{w}_2), s_1(\vec{w}_3), \dots s_M(\vec{w}_1), s_M(\vec{w}_2), s_M(\vec{w}_3)]^T. \quad (22)$$

The full information of the stack can be represented by its $3M \times 3M$-dimensional covariance matrix:

$$[R_p] = \langle \vec{y}_p \, \vec{y}_p^H \rangle. \quad (23)$$

$[R_p]$ can be expressed as the sum of a number of Kronecker products as:

$$[R_p] = \sum [C_3] \otimes [\Gamma_M]. \quad (24)$$

where $[C_3]$ are the conventional 3 x 3 polarimetric covariance matrices and $[\Gamma_M]$ the interferometric coherence matrices i.e. a $M \times M$ matrices that contain interferometric coherences between the acquisitions in the off-diagonal elements and ones in the diagonal. For the two-layer model-based inversion, only two Kronecker products are assumed to be sufficient to describe $[R_p]$, interpreted as the ground and the volume contributions [28]:

$$[R_p] = [C_{3G}] \otimes [\Gamma_{MG}] + [C_{3V}] \otimes [\Gamma_{MV}]. \quad (25)$$

The decomposition of (25) is intrinsically ambiguous: different $[\Gamma_{MG}]$, $[\Gamma_{MV}]$, $[C_{3G}]$ and $[C_{3V}]$ can be combined to provide the same $[R_p]$. A least squares optimisation can only provide candidate estimates of $[\Gamma_{MG}]$ and $[\Gamma_{MV}]$ [28]:

$$\begin{aligned} [\Gamma_{MG}](a) &= a[R_1] + (1-a)[R_2], \\ [\Gamma_{MV}](b) &= b[R_1] + (1-b)[R_2]. \end{aligned} \quad (26)$$

In (26), $[R_1]$ and $[R_2]$ are two $M \times M$-dimensional matrices obtained from the singular value decomposition of a permutated version of $[R_p]$ [28]. Precisely, they correspond to the left singular vectors associated to the largest two singular values. A formulation analogous to (26) can be obtained for the two candidate estimates of $[C_{MG}]$ and $[C_{MV}]$ using the right singular vectors. The scalars a and b vary in intervals that make the four matrices positive semi-definite and define the decomposition ambiguity. The availability of an increasing number of acquisitions allows to constrain the ambiguity but not to resolve it [29]. A unique solution can only be obtained by imposing physical constrains on the (interferometric) scattering scenario.

After applying the SKP decomposition on the polarimetric tomographic stack, the estimated "volume-only" interferometric coherence matrix $[\Gamma_{MV}]$ is used in the tomographic reconstruction (19) to obtain the "volume-only" $P_V(z)$ and the "ground-only" $P_G(z)$ vertical power profiles as:

$$\begin{aligned} P_V(z) &= \vec{h}(z)^H [\Gamma_{MV}] \vec{h}(z), \\ P_G(z) &= \vec{h}(z)^H [\Gamma_{MG}] \vec{h}(z). \end{aligned} \quad (27)$$

In addition to the inherent ambiguity in separating ground and volume components, a complete separation by means of (25) cannot be generally achieved. This is a consequence of the condition(s) imposed on the least squares optimisation, so that (26) should be interpreted as a maximisation/minimisation of the ground to volume ratio. In this sense, the volume component always contains a residual ground component and vice versa.

III. Forest Height Estimation

A. Single-baseline forest height inversion

In the context of a two-layer (volume-only and ground) inversion model the vertical reflectivity can be modelled as

$$F(z, \vec{w}) = f_V(z) + m(\vec{w}) \delta(z - z_0), \quad (28)$$

where $m(\vec{w})$ is the ground-to-volume ratio. Following the Random Volume over Ground (RVoG) model [11] [22] the volume-only reflectivity $f_V(z)$ is assumed to be polarisation-independent. The volume coherence $\tilde{\gamma}_{Vol}(k_z, \vec{w})$ is obtained by substituting (28) into (5):

$$\tilde{\gamma}_{Vol}(k_z, \vec{w}) = e^{j\varphi_0} \frac{\tilde{\gamma}_V(k_z) + m(\vec{w})}{1 + m(\vec{w})}, \quad (29)$$

where $\tilde{\gamma}_V(k_z)$ is the volume coherence:

$$\tilde{\gamma}_V(k_z) = \frac{\int_0^1 f_V(h_v z') \exp(j k_z h_v z') dz'}{\int_0^1 f_V(h_v z') \, dz'}. \quad (30)$$

The volume-only vertical power profile $P_V(z)$ of (27) is proposed in this paper as an approximation of volume-only vertical reflectivity for $f_V(h_v z')$ in (30) in normalised form.

In the two-layer model of (28) the ground-to-volume ratio $m(\vec{w})$ is the only polarisation-dependent parameter as the volume-only reflectivity profile $f_V(z)$ is assumed to be the same for each polarisation. As a consequence (29) can be rewritten in form of a line in the complex plane [7]:

$$\tilde{\gamma}_{\mathrm{Vol}}(k_z,\vec{w}) = e^{j\varphi_0}\left[\tilde{\gamma}_V(k_z) + L(\vec{w})\left(1-\tilde{\gamma}_V(k_z)\right)\right], \quad (31)$$

where $L(\vec{w}) = m(\vec{w})/(1+m(\vec{w}))$.

The inclination of the line on the complex plane, defined by the angle α, shown in Fig. 1, is independent of the ground-to-volume ratio $m(\vec{w})$ and, thus, the same for all polarisations $\tilde{\gamma}_{\mathrm{Vol}}(k_z,\vec{w})$. After compensating for the underlying ground phase term $\exp(j\varphi_0)$ and in the absence of any temporal decorrelation of the ground scattering component, it results:

$$\tan\alpha\,(k_z) = \frac{1-\mathrm{Re}\{\tilde{\gamma}_V(k_z)\}}{\mathrm{Im}\{\tilde{\gamma}_V(k_z)\}} = \frac{1-\mathrm{Re}\{\tilde{\gamma}_{\mathrm{Vol}}(k_z,\vec{w})\}}{\mathrm{Im}\{\tilde{\gamma}_{\mathrm{Vol}}(k_z,\vec{w})\}}. \quad (32)$$

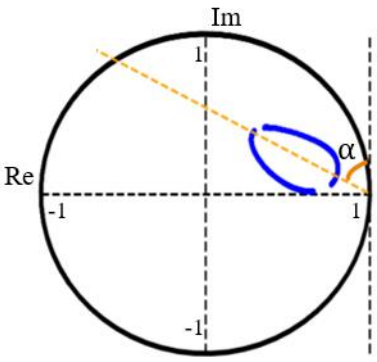

Fig. 1 Complex plane: a coherence region example for quad-polarimetric dataset with compensated ground phase is indicated by blue points and the Pol-InSAR line by the orange dashed line. The α-angle indicates the Pol-InSAR line inclination with respect to the vertical norm.

The inclination angle α depends only on the volume-only vertical reflectivity $f_V(z)$ and forest height h_v. Accordingly, if $f_V(z)$ is known, α depends only on h_v. This allows a significant simplification of the forest height inversion, which can now be treated as a single parameter problem and inverted by a single baseline, single polarisation acquisition $\tilde{\gamma}_{\mathrm{Vol}}(k_z,\vec{w})$:

$$h_v = \min_{h_v}\left\|\alpha(k_z \mid f_V(z), h_v) - \alpha(k_z,\vec{w})\right\|, \quad (33)$$

where $\alpha(k_z \mid f_V(z), h_v)$ is the forest height dependent model prediction:

$$\alpha(k_z \mid f_V(z), h_v) = \mathrm{atan}\left(\frac{1-\mathrm{Re}\{\tilde{\gamma}_V(k_z \mid f_V(z), h_v)\}}{\mathrm{Im}\{\tilde{\gamma}_V(k_z \mid f_V(z), h_v)\}}\right) \quad (34)$$

which is equal to the angle $\alpha(k_z,\vec{w})$ of any measured $\tilde{\gamma}_{\mathrm{Vol}}(k_z,\vec{w})$:

$$\alpha(k_z,\vec{w}) = \mathrm{atan}\left(\frac{1-\mathrm{Re}\{\tilde{\gamma}_{\mathrm{Vol}}(k_z,\vec{w})\}}{\mathrm{Im}\{\tilde{\gamma}_{\mathrm{Vol}}(k_z,\vec{w})\}}\right). \quad (35)$$

The inversion of (34) requires only a single-polarisation measurement. Polarisation diversity can be used to minimise estimation variance. One way to do this is to use the trace coherence $\tilde{\gamma}_{\mathrm{Trace}}(k_z)$ in (35), estimated from the normalised form of covariance matrix in (12) [24]:

$$\tilde{\gamma}_{\mathrm{Trace}}(k_z) = \mathrm{trace}([\Pi_{12}] - e^{j\varphi_0}[I]), \quad (36)$$

where [I] is the 3x3 unit matrix.

B. Multi-baseline forest height inversion

For repeat-pass InSAR implementations, as in the case of BIOMASS, the presence of temporal decorrelation imposes a critical limitation that requires in the best case a wider observation space for providing accurate forest height estimates. BIOMASS performs in the interferometric mission phase three quad-polarimetric acquisitions $s_i(\vec{w})$, acquired with a temporal baseline of three days [16]. These allow the formation of three repeat-pass interferograms.

The most common temporal decorrelation contribution over forested terrain for small and moderate temporal baselines is wind-induced decorrelation. The wind-induced moderate movement of tree elements of the canopy layer changes the location of the effective scatterers within the volume from acquisition to acquisition and introduces a non-volumetric decorrelation contribution on the interferometric coherence. In this case, however, both the scattering and propagation properties of the forest volume remain the same for all acquisitions [30].

Further assuming that the scattering properties of the ground do not change from acquisition to acquisition, implies in terms of (28) that the volume-only reflectivity profile $f_V(z)$ as well as the ground-to-volume ratio $m(\vec{w})$ remain the same for all acquisitions. The temporal decorrelation can be then described by a real polarisation independent decorrelation contribution γ_t and (29) modifies to [30] [31] [32]:

$$\tilde{\gamma}_{\mathrm{Vol}}(k_z,\vec{w}) = \exp(j\varphi_0)\,\frac{\gamma_t\tilde{\gamma}_V(k_z) + m(\vec{w})}{1+m(\vec{w})}. \quad (37)$$

In this case, the line equation (31) becomes

$$\tilde{\gamma}_{\mathrm{Vol}}(k_z,\vec{w}) = e^{j\varphi_0}[\gamma_t\tilde{\gamma}_V(k_z) + L(\vec{w})(1-\gamma_t\tilde{\gamma}_V(k_z))]. \quad (38)$$

After compensating the ground phase φ_0 and generalizing to the multi-baseline case, (37) modifies to:

$$\tilde{\gamma}_{\mathrm{Vol}}(k_z^{mn},\vec{w}) = \frac{\gamma_t^{mn}\tilde{\gamma}_{V0}(k_z^{mn}) + m(\vec{w})}{1+m(\vec{w})}, \quad (39)$$

where the temporal decorrelation γ_t^{mn} corresponds to the interferometric baseline with vertical wavenumber k_z^{mn}.

For a single polarisation $\vec{w}$, the three interferometric acquisitions lead to 3 interferometric coherences $\{\tilde{\gamma}_{\mathrm{Vol}}^{12}(k_z^{12},\vec{w}), \tilde{\gamma}_{\mathrm{Vol}}^{13}(k_z^{13},\vec{w}), \tilde{\gamma}_{\mathrm{Vol}}^{23}(k_z^{23},\vec{w})\}$ associated to a set of vertical wavenumbers $\{k_z^{12}, k_z^{13}, k_z^{23}\}$. If the volume-only vertical reflectivity profile is parameterised by an exponential function with corresponding extinction coefficient σ [5], the forest height inversion problem can be formulated in terms of a minimisation problem for six parameters: forest height, ground-to-volume ratio, extinction coefficient and three temporal decorrelations:

$$\{h_v, m, \sigma, \gamma_t^{12}, \gamma_t^{13}, \gamma_t^{23}\} = \arg \min_{h_v, m, \sigma, \gamma_t^{12}, \gamma_t^{13}, \gamma_t^{23}} \left\| \begin{bmatrix} \tilde{\gamma}_{Vol}(k_z^{12}, \vec{w}) \\ \tilde{\gamma}_{Vol}(k_z^{13}, \vec{w}) \\ \tilde{\gamma}_{Vol}(k_z^{23}, \vec{w}) \end{bmatrix} - \begin{bmatrix} \tilde{\gamma}_{Vol}(k_z^{12}, \{h_v, m, \sigma, \gamma_t^{12}\}) \\ \tilde{\gamma}_{Vol}(k_z^{13}, \{h_v, m, \sigma, \gamma_t^{13}\}) \\ \tilde{\gamma}_{Vol}(k_z^{23}, \{h_v, m, \sigma, \gamma_t^{23}\}) \end{bmatrix} \right\|. \quad (40)$$

The knowledge about the vertical profiles allows to reduce the dimensionality of the minimisation problem (40) as profile parameter σ can be excluded from the estimation:

$$\{h_v, m, \gamma_t^{12}, \gamma_t^{13}\} = \arg \min_{h_v, m, \gamma_t^{12}, \gamma_t^{13}} \left\| \begin{bmatrix} \tilde{\gamma}_{Vol}(k_z^{12}, \vec{w}) \\ \tilde{\gamma}_{Vol}(k_z^{13}, \vec{w}) \end{bmatrix} - \begin{bmatrix} \tilde{\gamma}_{Vol}(k_z^{12}, \{h_v, m, \gamma_t^{12}\}) \\ \tilde{\gamma}_{Vol}(k_z^{13}, \{h_v, m, \gamma_t^{13}\}) \end{bmatrix} \right\|. \quad (41)$$

In (41), the look-up-table (LUT) required to invert the forest height has only 4 dimensions, whereas in (40) it has 6 dimensions. It allows to significantly improve the computational time.

IV. Experimental data

The quad-polarimetric tomographic data used in the following were acquired in February 2016 by DLR's F-SAR airborne sensor over the Lopé site in Gabon in the frame of the AfriSAR campaign [33] [34].

The Lopé site is located within the Lopé National Park in Gabon. The site features a variety of structure types ranging from open savannas to undisturbed tall (sometimes exceeding 50 m) dense forest stands [35] [36].The terrain is hilly with many local slopes steeper than 20°.

Airborne Lidar data are used as a reference, collected by NASA's Land, Vegetation, and Ice Sensor (LVIS) in February 2016 as well [37]. LVIS measures wide-beam full-waveforms footprints of approximately 22 m in diameter. From the measured waveforms the RH100 estimates (i.e. the height in meters from the ground where 100% of energy return occurs [38]) are derived, interpolated and resampled to a 20 m x 20 m grid and finally transformed in UTM-coordinates (shown in the top plot of Fig. 2 together with the Lidar Digital Terrain Model, DTM, in the middle plot). They are used as the reference forest height h_v^{ref}.

The 12m resolution TanDEM-X digital elevation model (DEM) is used as a topographic reference height z_{DEM} [39] [40] [41]. The non-forested area is masked out by using the global TanDEM-X forest / non-forest map [42], shown in the bottom plot of Fig. 2.

Following the processing steps described in Section II, 100 looks fully polarimetric tomographic covariance matrices $[R_p]$ are formed, geocoded in UTM coordinates and resampled to a 20 m x 20 m grid. They are used to estimate both ground and volume coherence matrices by SKP decomposition, $[\Gamma_{MG}]$ and $[\Gamma_{MV}]$, taking the solutions closer to the coherence region [29] [43]. The associated ground- and volume-only power profiles, $P_G(z)$ and $P_V(z)$, are produced according to (27) using the Fourier beamforming reconstruction algorithm.

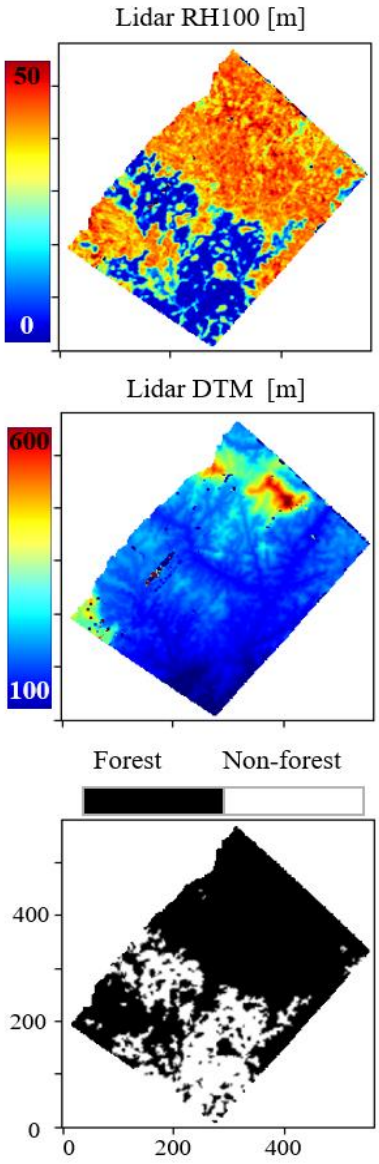

Fig. 2 Lopé test site, from top to bottom: LVIS LiDAR RH100 Forest height, LVIS Lidar digital terrain model (DTM) and Forest-non-Forest map derived from Tandem-X data. The axis denote pixels with size of 20 m x 20 m.

The underlying ground elevation z_0 and the phase φ_0 associated to it is then estimated from the lowest peak in the ground-only vertical power profile $P_G(z)$ within the interval of $z_{DEM} - 50m < z < z_{DEM} + 30m$ as described in [44], [45].

In order to use the derived volume-only power profiles $P_V(z)$ in (30), they have to be cropped and normalised. The lower cropping boundary is the position of the estimated ground phase. The upper boundary is estimated from the volume-only

vertical power profiles from the position of 3dB attenuation of the highest peak within the interval of $z_{DEM} - 50m < z < z_{DEM} + 30m$. The cropped profiles are then resampled to the normalised unit height axis to obtain the normalised volume-only vertical power profiles.

V. Results

The different inversion scenarios discussed in Chapter III are applied on the experimental data described in Section IV. First, the insufficiency of directly using the tomographically reconstructed vertical power profile $P(z_i, \vec{w})$ (see (19)) to represent the vertical reflectivity $F(z, \vec{w})$ in (5) is demonstrated. For this, the normalised $P(z_i, \vec{w})$ profiles are substituted into (5) in order to obtain a prediction for the complex volume decorrelation contribution:

$$\tilde{\gamma}_{Vol}^{P}(k_z, \vec{w}) = \frac{\int_0^1 P(h_v z', \vec{w})\, e^{jk_z h_v^{ref} z'} dz'}{\int_0^1 P(h_v z', \vec{w})\, dz'} \quad (42)$$

using the lidar RH100 reference height h_v^{ref}. The so obtained $\tilde{\gamma}_{Vol}^{P}(k_z, \vec{w})$ predictions are compared in terms of absolute volumetric decorrelation $|\tilde{\gamma}_{Vol}^{P}(k_z, \vec{w})|$, phase center $\varphi^P = \arctan\left(Im\{\tilde{\gamma}_{Vol}^{P}(k_z, \vec{w})\}\right)/Re\{\tilde{\gamma}_{Vol}^{P}(k_z, \vec{w})\}\right)$ and line inclination angle $\alpha^P = \arctan\left(\left(1 - Re\{\tilde{\gamma}_{Vol}^{P}(k_z, \vec{w})\}\right)/ Im\{\tilde{\gamma}_{Vol}^{P}(k_z, \vec{w})\}\right)$ against the measured $|\tilde{\gamma}_{Vol}(k_z, \vec{w})|$, $\varphi = \arctan\left(Im\{\tilde{\gamma}_{Vol}(k_z, \vec{w})\}\right)/Re\{\tilde{\gamma}_{Vol}(k_z, \vec{w})\}\right)$ and $\alpha = \arctan\left(\left(1 - Re\{\tilde{\gamma}_{Vol}(k_z, \vec{w})\}\right)/Im\{\tilde{\gamma}_{Vol}(k_z, \vec{w})\}\right)$.

The top row of Figure 3 shows that both the measured and the predicted absolute volumetric decorrelation decrease with increasing $k_z h_v^{ref}$ (left and middle plot) within 0 and 2π. However, the measured coherence is systematically lower, denoting the presence of a scattering contribution not well captured by the prediction. The fact that the measured phase center is lower than the predicted one (second row) indicates that the scattering contribution missed by the prediction is likely located at the ground level. In contrast, the predicted α-angle fits well to the measured one. These results confirm experimentally the expected invariance of the α-angle to the presence of a stronger or weaker (Dirac-like) ground response.

Furthermore, the two different curves of φ^P behaviour with respect to $k_z h_v^{ref}$ are visible in the middle row, middle column of Fig.3. At larger values of $k_z h_v^{ref}$, the φ^P values demonstrate two distinct behaviors: one where φ^P increases rapidly with of $k_z h_v^{ref}$, and another where φ^P increases more slowly and almost linearly with $k_z h_v^{ref}$. While the former behaviour corresponds to vertical power profiles with larger power values closer to the canopy (top), the latter corresponds to rather uniform vertical power profiles from the canopy top to the ground. Such profiles are either produced for shorter forest stands due to low vertical resolution or at larger positive slopes. For α^P, these two curves merge closer together.

Next, the forest height inversion performance is assessed for the single- and multi-baseline case. For this, three interferometric image pairs with different vertical wavenumbers k_z chosen to fit the BIOMASS observation scenario are used. The corresponding vertical wavenumber maps are shown in top row of Fig. 4: for the first one (left column - smaller k_z), the vertical wavenumber k_z varies between 0.04 and 0.08 rad/m (increasing from far to near range as a result of the incidence angle variation), for the second one (middle column - middle k_z) between 0.07 and 0.11 rad/m while for the third one (right column - larger k_z) between 0.10 and 0.15 rad/m.

The inversion performance is assessed against the lidar RH100 reference height h_v^{ref} using the Root Mean Square Error metric $RMSE = \sqrt{\sum(h_v - h_v^{ref})^2}$ and the coefficient of determination $r^2 = 1 - \sum\left(h_v - h_v^{ref}\right)^2 / \sum\left(h_v - \bar{h}_v\right)^2$ where h_v are the height estimates and $\bar{h}_v$ the mean estimated height. At the same time maps of the absolute error $h_v - h_v^{ref}$ are shown in the middle and bottom rows of Fig. 4, while the validation histograms are shown in Fig. 5.

The single-baseline inversion performance achieved using the original tomographically reconstructed vertical power profile $P(z_i, HV)$ for each of the three interferometric pairs is shown in the middle row of Fig. 4 and top row of Fig. 5 (with increasing vertical wavenumber from left to right). For the smaller k_z (left) the obtained heights are clearly overestimated with $RMSE = 7.88$ m and $r^2 = -1.5$. The performance improves at the middle k_z with RMSE=4.24 m and $r^2 = 0.13$, but the obtained heights continue to be overestimated across the whole height range. For the larger k_z, the obtained heights (with an overall RMSE=7.82 m and $r^2 = -1.2$) remain overestimated up to a height of about 25 m, while taller heights are underestimated as a result of the lower height sensitivity at this large vertical wavenumber range.

The overall overestimation is a direct result of the structural misfit between the underlying vertical reflectivity profile and the used tomographically reconstructed vertical power profile $P(z_i, HV)$. The single-baseline inversion performance achieved for each of the three interferometric pairs by using the volume-only vertical power profile $P_V(z_i)$ is shown in the bottom rows of Figs. 5 and 6. The performance improvement, even if this is not fully reflected in the RMSE and coefficient of determination values (with a $RMSE = 5.59$ m and $r^2 = 0.27$ for the smaller k_z, $RMSE = 4.25$ m and $r^2 = 0.28$ for the middle and $RMSE = 7.36$ m and $r^2 = -0.6$ for the larger k_z) is significant: the overestimation is compensated across the whole height range (of course within the limits imposed by the individual vertical wavenumbers) indicating a better if not optimum modelling of the vertical reflectivity profile.

To investigate the importance of profile diversity, the forest height inversion is repeated using only a single "mean" profile for the entire acquisition scene. This "mean" profile represents the most dominant component in the profiles and its derivation

is described in [9] [46]. For the single profile inversion, using a single-baseline with middle vertical wavenumbers values $k_z \approx 0.7 \ldots 0.11$, the RMSE is equal to 3.65 m and $r^2 = 0.28$ as in the bottom left column of Fig. 6.

Finally, the multi-baseline Pol-InSAR inversion scenario allows to account for the other model parameters affecting the volumetric decorrelation, e.g. temporal decorrelations and structural parameters. Following (41), four parameters are estimated including the forest height, the ground-to-volume ratio and two temporal decorrelation values, one for each of the two baselines. With the volume-only reflectivity profile the inversion results in $\mathrm{RMSE} = 4.79$ and $r^2 = 0.40$ as presented in middle column of Fig. 6.

The inversion scenario with three interferometric acquisitions and known vertical power profile $P_V(z_i)$ is finally compared to the more standard inversion using the exponential profile for the parameterisation of volume-only vertical reflectivity profile and overall six unknown parameters, i.e. forest height, the three ground-to-volume ratios, extinction coefficient and three temporal decorrelations. Following (40) the performance is presented in right column of Fig. 6, with $\mathrm{RMSE} = 9.12$ and $r^2 = -1.7$.

VI. Discussion and Conclusion

Today, a number of planned spaceborne SAR missions complement their interferometric measurements with a tomographic operation phase. One of the objectives of this work was to establish connections between the tomographic and interferometric phases of a given mission by identifying possible synergies. ESA's BIOMASS mission serves as a reference mission that combines both tomographic and interferometric phases. It is important to note here that this does not imply that the performance achieved is characteristic of BIOMASS, as key data quality parameters such as spatial resolution, noise level (NESZ), etc., have not been adapted. It is rather the BIOMASS mission design, in terms of its observation space and the acquisition scenario, is used as a framework for addressing the proposed methodology.

The most apparent synergy between the tomographic and interferometric mission phases is the estimation of ground topography. Firstly, a tomographic or multi-baseline estimation (performed during the tomographic phase) is expected to be more accurate than an estimation with fewer (interferometric) acquisitions, as conducted during the interferometric phase. Secondly, ground topography is the only parameter that can be assumed to remain invariant over the lifetime of a mission.

For the forest height inversion, knowledge of ground topography is essential, as it restricts the possible solution space by fixing the lower boundary of the problem. However, even in the absence of ground topography information, the conclusions of this work remain valid. The observation space provided by the number of interferometric acquisitions necessary for the height inversion (at least one in the absence of temporal decorrelation and at least two in its presence), allows for the estimation of ground topography using conventional inversion method(s). In this case, the availability of polarimetric diversity in the interferometric measurements is required, which is also necessary for ground and volume separation.

Besides knowledge of the underlying ground, the performance of model-based forest height inversion from single- and multi-baseline Pol-InSAR coherence measurements strongly depends on the definition or parameterisation of the vertical reflectivity profile, especially at lower frequencies where attenuation is low(er) and ground scattering contributions become more relevant. To address this, the use of the tomographically reconstructed reflectivity profile is proposed. However, the conventional full vertical reflectivity profile reconstruction is insufficient for coherence-based forest height inversion. The primary reason for this insufficiency lies in the low vertical resolution of the reconstruction, inherent in any actual space-borne tomographic data set due to the limited number of tomographic acquisitions possible. This limitation impacts the Dirac-like ground response, causing it to be smeared out and become volume-like contributions superimposing the volume part of the profile. This insufficiency of the tomographically reconstructed vertical reflectivity profile to describe the interferometric (volume) coherences has been addressed in terms of the ground and volume separation.

When the vertical volume-only reflectivity (along with the underlying topography) is known, the single-baseline inversion reduces to a single-parameter problem (in the absence of temporal decorrelation). To achieve this, the inversion can be addressed by means of the line inclination angle α of the coherence line on the complex plane. This estimate is independent of the polarisation (e.g. the ground-to-volume ratio) and, in the absence of temporal decorrelation, depends solely on the forest height. It shows strong correlation with the estimate α^P derived from the predicted volumetric decorrelation $\tilde{\gamma}_{\mathrm{Vol}}^{P}(k_z, \vec{w})$ calculated using tomographic vertical power profiles. Apart from a more accurate description of the volume reflectivity, the proposed approach simplifies the inversion problem, leading to faster computation times, whether addressing the problem with temporal decorrelation or in its absence.

The reconstructed reflectivity profile of the volume-only component cannot be assumed without reservations to be invariant in time. At P-band it can change moderately as a result of dielectric changes occurring due to seasonal variations or weather effects (e.g. rain or draughts) or more significantly due to forest management or disturbances. Dielectric changes primarily affect the ground-to-volume ratio and are largely compensated by the separation of the ground scattering component. The height estimation, using the proposed approach, remains independent of any (residual) ground-to-volume ratio. Of course, significant changes of the shape of the underlying reflectivity profile lead to estimation biases.

For shorter stands (below 30m), the use of tomographic vertical power profiles is less effective due to limited vertical resolution. Also, the forest height inversion performance is affected by temporal decorrelation. To account for temporal decorrelation, a multi-baseline inversion algorithm that considers temporal decorrelation is employed. At the same time, when using a 3-acquisition inversion with temporal decorrelation and a classic exponential profile, a consistent bias is observed, leading to an underestimation of forest height, even for shorter stands. It is also worth noting that shorter trees are not representative of the Lopé test site, as they comprise only a small percentage of the stands and are primarily located on the forest/savannah boundaries.

Nevertheless, the sensitivity of the interferometric coherence to the shape of the vertical reflectivity profile is less pronounced than its sensitivity to the forest height itself. Accordingly, the low vertical resolution of the volume-only vertical power profile is of minor importance for the accuracy of the forest height estimation, especially when compared to the advantages and the flexibility that an inversion with a known profile provides. However, a significant mismatch between the reconstructed and actual vertical reflectivity profile will result in a biased height inversion, but will still permit valuable estimates of height change.

In this case, techniques that allow to estimate the vertical reflectivity profile from a limited number of inteferometric acquisitions, such as Polarisation Coherence Tomography (PCT) [47], may be an alternative. However, their conventional implementation is also associated with a number of constraints and challenges, as they require not only the knowledge of the underlying ground topography but also of the forest height. At the same time, they provide vertical reflectivity profiles that are not always physical as there is an infinite number of vertical reflectivity profiles that can reproduce a finite number of coherences. Alternatively, other high-resolution vertical power profile reconstruction techniques, such as Compressive Sensing [48], could be considered as a future enhancement of the described methodology.

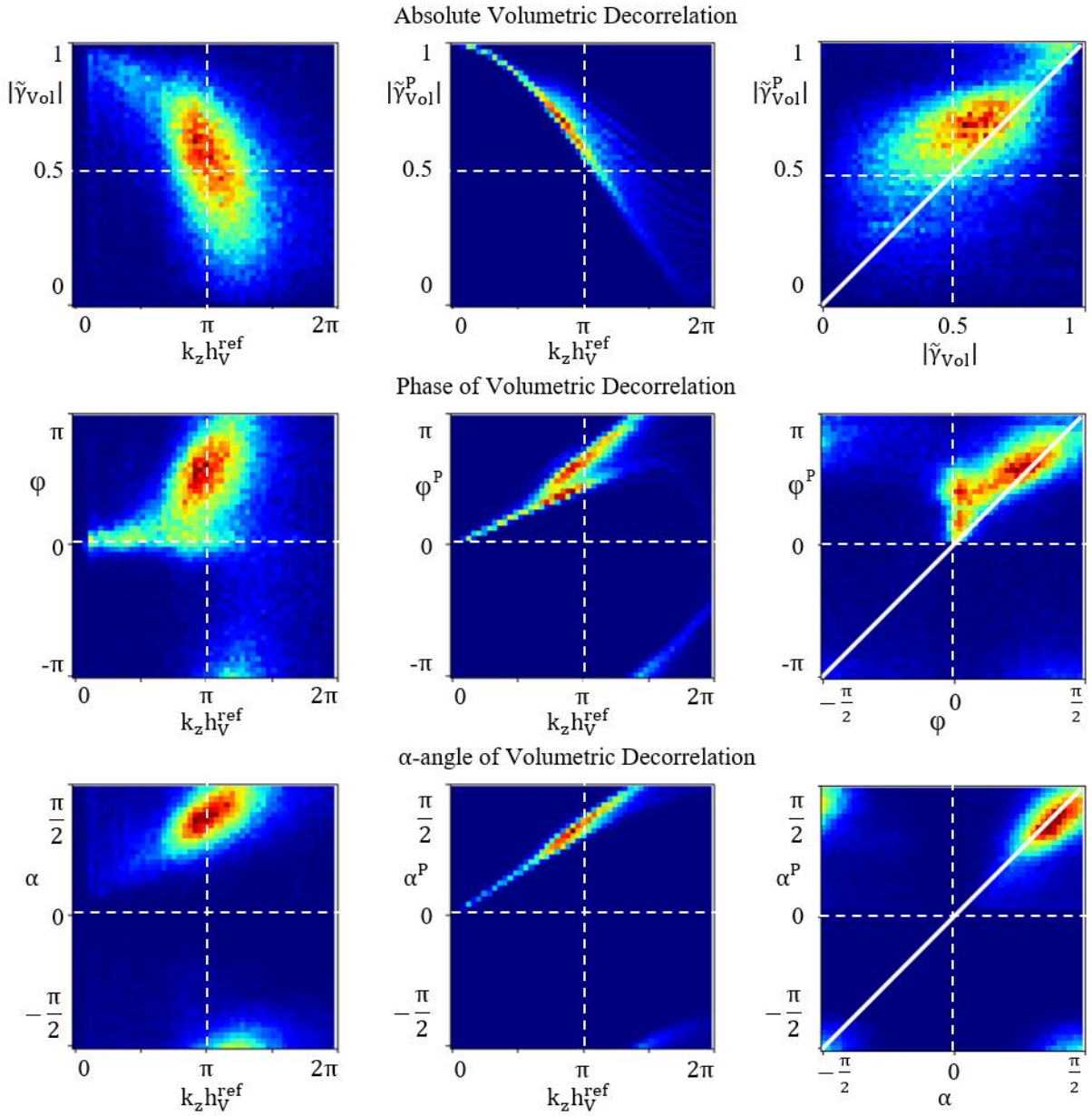

Fig. 3 Left column: correlation histograms from top to bottom: HV-polarised interferometric coherence $\left|\tilde{\gamma}_{Vol}(k_z, \vec{w})\right|$, phase center φ , and line inclination angle α against the product $k_z h_v^{ref}$. Middle column: correlation histograms, from top to bottom: predicted interferometric coherence $\left|\tilde{\gamma}^{P}_{Vol}(k_z, \vec{w})\right|$, predicted phase center φ^{P}, and predicted line inclination angle α^{P} against $k_z h_v^{ref}$. Right column: correlation histograms, from top to bottom: predicted interferometric coherence, predicted phase center, and predicted line inclination angle against interferometric coherence, phase center, and line inclination angle.

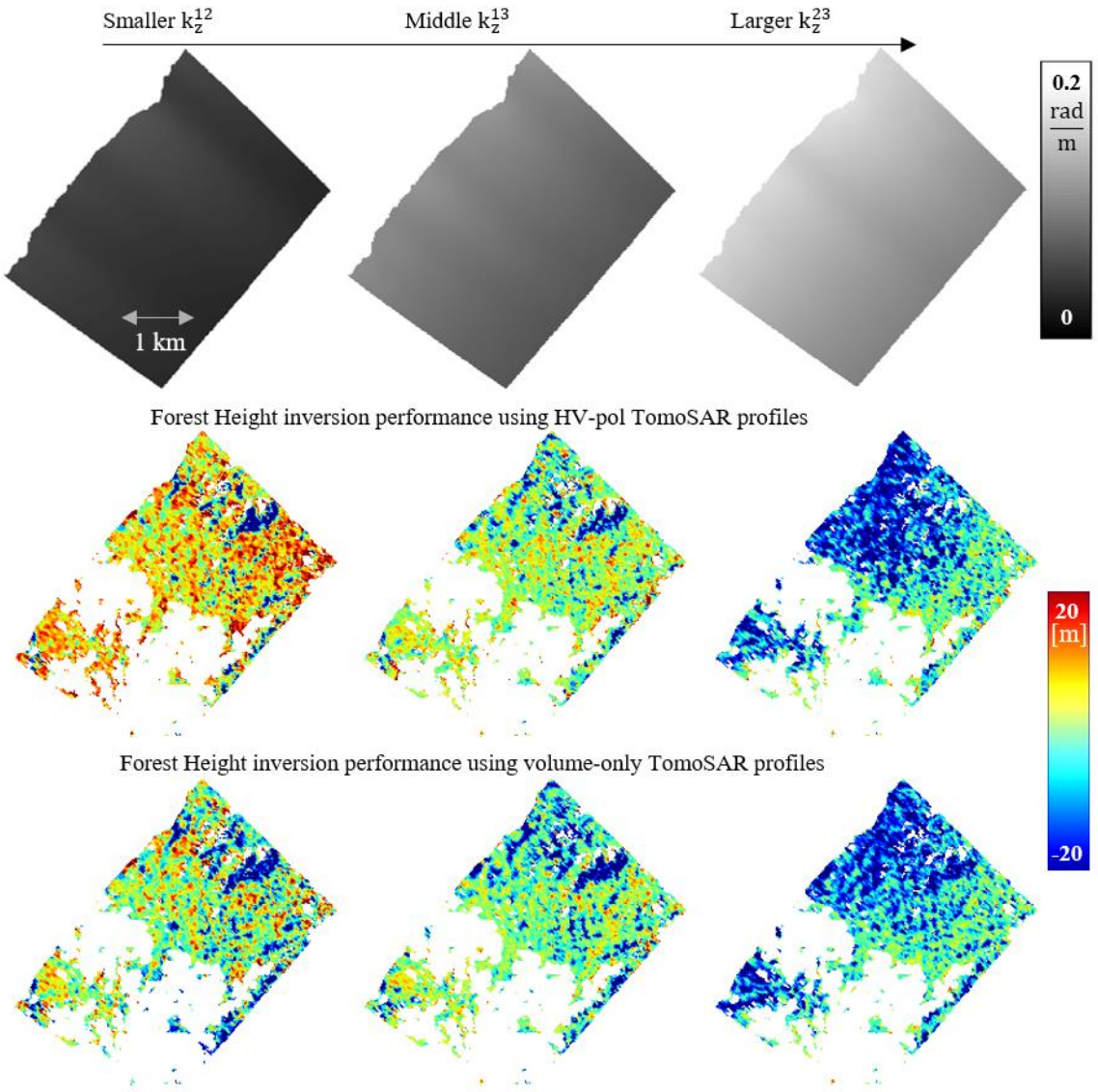

Fig. 4 Top row: Three ranges of k_z in [rad/m] for three F-SAR interferometric acquisitions in the Lopé test site. Middle and bottom rows: Lopé forest height error maps with respect to LiDAR RH100 reference in meters. Middle row: Single-baseline inversion using HV-polarised TomoSAR profiles corresponding to smaller, middle, and larger k_z. Bottom row: Single-baseline inversion using SKP separated volume-only TomoSAR profiles corresponding to smaller, middle, and larger k_z.

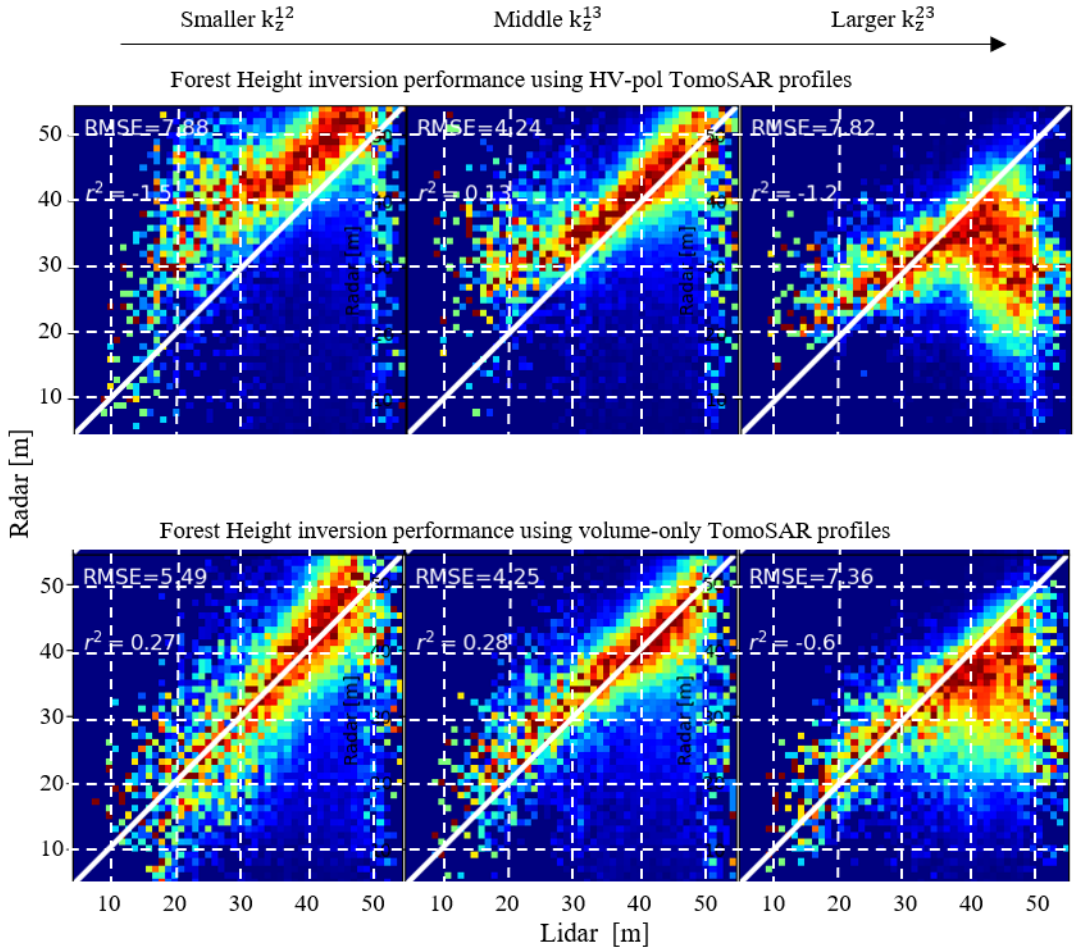

Fig. 5 Lopé forest height validation histograms relative to LiDAR RH100 reference. Top row: Single-baseline inversion using HV-polarised TomoSAR profiles for three different ranges of vertical wavenumber k_z, from left to right: smaller, middle, and larger k_z. Bottom row: Single-baseline inversion using SKP separated volume-only TomoSAR profiles, corresponding to three different ranges of vertical wavenumber k_z, from left to right: smaller, middle, and larger k_z.

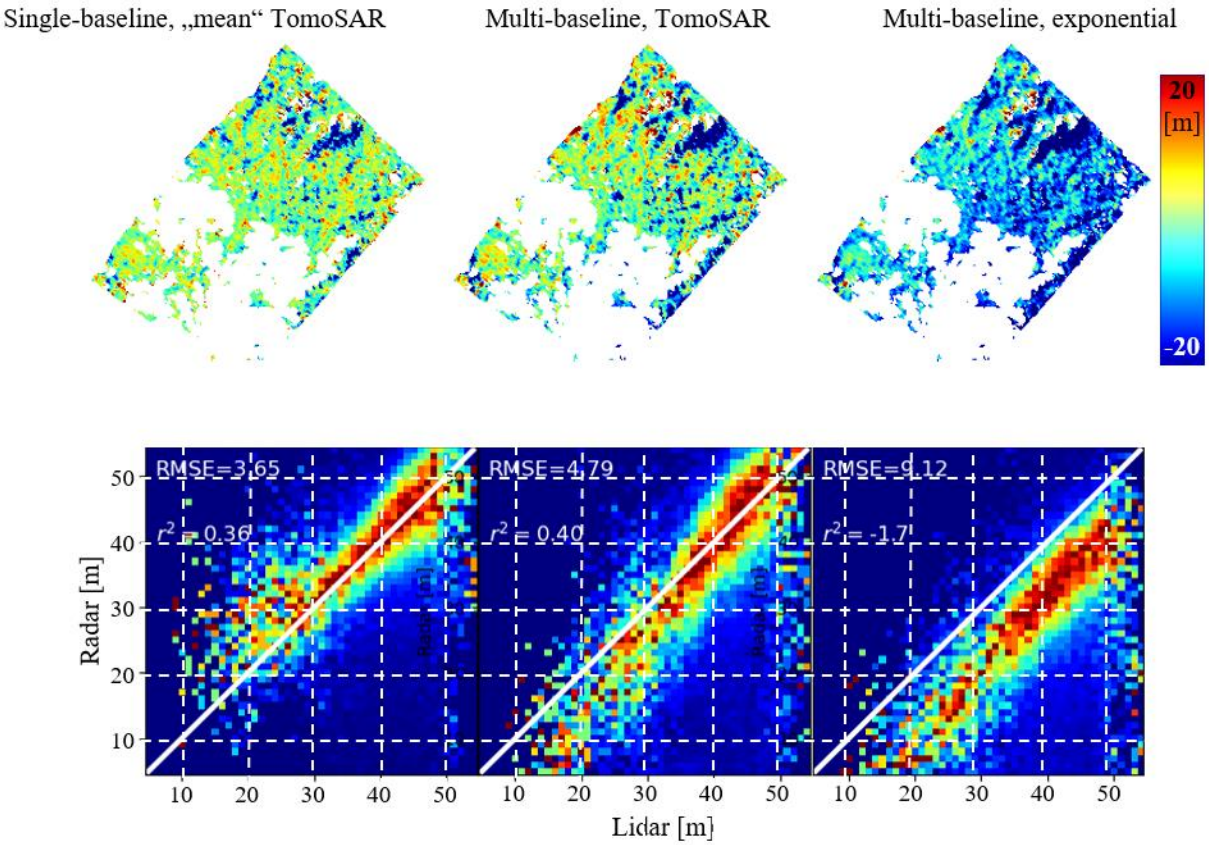

Fig. 6 Top row: Lopé forest height error maps with respect to LiDAR RH100 reference in meters. Bottom row: Validation histograms relative to LiDAR RH100 reference. Left column: Single-baseline inversion using SKP separated volume-only "mean" TomoSAR profile for the middle range of k_z. Middle column: 3 acquisitions inversion using SKP separated volume-only TomoSAR profiles. right column: 3 acquisitions inversion with classic approach using exponential function as an approximation to the vertical reflectivity and 6 inversion parameters.

ACKNOWLEDGMENT

Data sets were provided by the Land, Vegetation and Ice Sensor (LVIS) team in Code 61A at NASA Goddard Space Flight Center with support from the University of Maryland, College Park. The authors would also like to acknowledge the F-SAR team for their invaluable efforts during the data acquisition and processing.

REFERENCES

[1] H. Pretzsch, "Forest Dynamics, Growth and Yield: From Measurement to Model," *Berlin, Germany: Springer-Verlag,* 2009.

[2] T. Mette, K. Papathanassiou, I. Hajnsek, H. Pretzsch and P. Biber, "Applying a common allometric equation to convert forest height from Pol-InSAR data to forest biomass," in *IEEE IGARSS*, Anchorage, AK, USA, 2004.

[3] F. G. Hall et al., "Characterizing 3D vegetation structure from space: Mission requirements," *Remote Sens. Environ.,* vol. 115, no. 11, p. 2753–2775, 2011.

[4] F. Kugler, S.-K. Lee and K. Papathanassiou, "Forest Height Estimation by means of Pol-InSAR Data Inversion: The Role of the Vertical Wavenumber," *IEEE Trans. Geosci. Remote Sens.,* vol. 53, no. 10, 2015.

[5] S. Cloude and K. Papathanassiou, "Three-stage inversion process for polarimetric SAR interferometry," *IEEE Proc. – Radar Sonar Navig,* vol. 150, no. (3), pp. 125-134, 2003.

[6] S. Cloude and K. Papathanassiou, "Polarimetric SAR interferometry," *IEEE Trans. Geosci. Remote Sens.,* vol. 36, no. 5, pp. 1551-1565, 1998.

[7] K. Papathanassiou and S. Cloude, "Single-baseline polarimetric SAR interferometry," *IEEE Trans. Geosci. Remote Sens,* vol. 39, no. 11, pp. 2352-2363, 2001.

[8] G. Krieger, K. P. Papathanassiou and S. R. Cloude, "Spaceborne polarimetric SAR interferometry: performance analysis and mission concepts," *EURASIP J. Applied Sig. Proc. 20,* pp. 3272-3292, 2005.

[9] R. Guliaev, V. Cazcarra-Bes, M. Pardini and K. Papathanassiou, "Forest Height Estima-tion by Means of TanDEM-X InSAR and Wave-form Lidar Data.," *IEEE Journal of Selected Topics in Applied Earth Observations and Remote Sensing,* vol. 14, pp. 3084-3094, 2021.

[10] F. Garestier, P. Dubois-Fernandez and I. Champion, "Forest height inversion using high-resolution P-band Pol-InSAR data," *IEEE Transactions on Geoscience and Remote Sensing,* vol. 46, no. 11, pp. 3544-3559, 2008.

[11] R. Treuhaft and P. Siqueira, "Vertical structure of vegetated land surfaces from interferometric and polarimetric radar," *Radio Science,* vol. 35, no. 1, pp. .141-177, 2000.

[12] J. Askne, P. Dammert, L. Ulander and G. Smith, "C-band repeat-pass interferometric SAR observations of the forest," *IEEE Transactions on Geoscience and Remote Sensing,* vol. 35, no. 1, pp. 25-35, 1997.

[13] F. Garestier, P. Dubois-Fernandez and K. Papathanassiou, "Pine forest height inversion using single-pass X-band PolInSAR data," *IEEE Transactions on Geoscience and Remote Sensing,* vol. 46, no. 1, pp. 59-68, 2007.

[14] M. Schlund, P. Magdon, B. Eaton, C. Aumann and S. Erasmi, "Canopy height estimation with TanDEM-X in temperate and boreal forests," *International Journal of Applied Earth Observation and Geoinformation,* vol. 82, p. 101904, 2019.

[15] M. Soja, H. Persson and L. Ulander, "Modeling and detection of deforestation and forest growth in multitemporal TanDEM-X data," *IEEE Transactions on Geoscience and Remote Sensing,* vol. 11, no. 10, pp. 3548-3563, 2018.

[16] S. Quegan, T. Le Toan, J. Chave, J. Dall, J. Exbrayat, D. Minh, M. Lomas, M. D'alessandro, P. Paillou, K. Papathanassiou and F. Rocca, "The European Space Agency BIOMASS mission: Measuring forest above-ground biomass from space," *Remote Sensing of Environment,* no. 227 , pp. 44-60, 2019.

[17] A. Moreira, G. Krieger, I. Hajnsek, K. Papathanassiou, M. Younis, P. Lopez-Dekker, S. Huber, M. Villano, M. Pardini, M. Eineder and F. De Zan, "Tandem-L: A highly innovative bistatic SAR mission for global observation of dynamic processes," *IEEE Geoscience and remote sensing magazine,* vol. 3, no. 2, pp. 8-23, 2015.

[18] H. Zebker and J. Villasenor, "Decorrelation in interferometric radar echoes," *IEEE Transactions on geoscience and remote sensing,* vol. 30, no. 5, pp. 950-959., 1992.

[19] J. Hagberg, L. Ulander and J. Askne, "Repeat-pass SAR interferometry over forested terrain," *IEEE Transactions on Geoscience and Remote Sensing,* vol. 33, no. 2, pp. 331-340., 1995.

[20] C. Hao, S. Cloude and J. White, "Using GEDI Waveforms for Improved Tan-DEM-X Forest Height Mapping: A Combined SINC+ Legendre Approach," *Remote Sensing,* vol. 13, no. 15 , p. 2882, 2021.

[21] Z. Liao, B. He, A. I. van Dijk, X. Bai and X. Quan, "The impacts of spatial baseline on forest canopy height model and digital terrain model retrieval using P-band PolInSAR data," *Remote Sensing of Environment,* vol. 210, pp. 403-421, 2018.

[22] S. Cloude, Polarisation: applications in remote sensing, Oxford: OUP , 2009.

[23] T. Flynn, M. Tabb and R. Carande, "Coherence region shape extraction for vegetation parameter estimation in polarimetric SAR interferometry. In IEEE International Geoscience and Remote Sensing Symposium," in *IEEE International Geoscience and Remote Sensing Symposium*, Toronto, ON, Canada, 2002.

[24] A. Marino, "Trace Coherence: A New Operator for Polarimetric and Interferometric SAR images," *IEEE Transactions on Geoscience and Remote Sensing,* vol. 55, no. 4, pp. 2326-2339, April 2017.

[25] F. Lombardini and A. Reigber, "Adaptive spectral estimation for multibaseline SAR tomography with airborne L-band data," in *IEEE International Geoscience and Remote Sensing Symposium*, 2003.

[26] V. Cazcarra-Bes, M. Pardini, M. Tello and K. Papathanassiou, "Comparison of tomographic SAR reflectivity reconstruction algorithms for forest applications at L-band," *IEEE Transactions on Geoscience and Remote Sensing,* vol. 58, no. 1, pp. 147-164, 2019.

[27] A. Reigber and A. Moreira, " First demonstration of air-borne SAR tomography using multibaseline L-band data," *IEEE Trans. Geosci. Remote Sens.,* vol. 38, no. 5, pp. 2142-2152, Sept. 2000.

[28] S. Tebaldini, "Algebraic synthesis of forest scenarios from multibaseline PolInSAR data," *IEEE Transactions on Geoscience and Remote Sensing,* vol. 47, no. 12, pp. 4132-4142, 2009.

[29] S. Tebaldini and F. Rocca, "Multibaseline polarimetric SAR tomography of a boreal forest at P-

and L-bands," *IEEE Transactions on Geoscience and Remote Sensing,* vol. 50, no. 1, pp. 232-246, 2011.

[30] K. Papathanassiou and S. Cloude, "The effect of temporal decorrelation on the inversion of forest parameters from Pol-InSAR data," in *International Geoscience and Remote Sensing Symposium*, 2003.

[31] M. Lavalle and K. Khun, "Three-baseline InSAR estimation of forest height," *IEEE Geoscience and Remote Sensing Letters,* vol. 11, no. 10, pp. 1737-1741, 2014.

[32] S. Lee, F. Kugler, K. Papathanassiou and I. Hajnsek, "Quantification of temporal decorrelation effects at L-band for polarimetric SAR interferometry applications," *IEEE Journal of Selected Topics in Applied Earth Observations and Remote Sensing,* 2013.

[33] I. Hajnsek, M. Pardini, et al.,, "Technical assistance for the development of airborne SAR and geophysical measurements during the AfriSAR campaign, Final technical report".

[34] T. Fatoyinbo et al., "The NASA AfriSAR campaign: Airborne SAR and lidar measurements of tropical forest structure and biomass in support of current and future space missions," vol. 264, p. 112533, 2021.

[35] N. Labriere et al, "In Situ Reference Datasets from the TropiSAR and AfriSAR Campaigns in Support of Upcoming Spaceborne Biomass Missions," *IEEE J. Sel. Top. Appl. Earth Obs. Remote Sens,* vol. 11, no. 10, p. 3617–3627, 2018.

[36] S. M. Marselis, H. Tang, J. D. Armston, K. Calders, N. Labrière and R. Dubayah, "Distinguishing vegetation types with airborne waveform lidar data in a tropical forest-savanna mosaic: A case study in Lopé National Park, Gabon," *Remote Sens. Environ,* vol. 216, no. 626–634, 2018.

[37] J. Blair and M. Hofton, "AfriSAR LVIS L2 Geolocated Surface Elevation Product, Version 1. Boulder, Colorado USA. NASA National Snow and Ice Data Center Distributed Active Archive Center," [Online]. [Accessed 2018].

[38] R. O. Dubayah et al., "Estimation of tropical forest height and biomass dynamics using lidar remote sensing at La Selva, Costa Rica," *," J. Geophys Res.,* vol. 115, 2010.

[39] B. Wessel, "TanDEM-X ground segment–DEM products specification document," 2018.

[40] M. Zink et al, "TanDEM-X: The New Global DEM Takes Shape," *," in IEEE Geoscience and Remote Sensing Magazine,* vol. 2, no. 2, 2014.

[41] P. Rizzoli et al., "Generation and performance assessment of the global TanDEM-X digital elevation model," *ISPRS Journal of Photogrammetry and Remote Sensing,* vol. 132, pp. 119-139, 2017.

[42] M. Martone, P. Rizzoli, C. Wecklich, C. González, J.-L. Bueso-Bello, P. Valdo, D. Schulze, M. Zink, G. Krieger and A. Moreira, "The global forest/non-forest map from TanDEM-X interferometric SAR data," *Remote Sensing of Environment,* vol. 205, pp. 352-373, 2018.

[43] M. Pardini and K. Papathanassiou, "On the estimation of ground and volume polarimetric covariances in forest scenarios with SAR tomography," *IEEE Geoscience and Remote Sensing Letters,* vol. 14, no. 10, pp. 1860-1864, 2017.

[44] M. Pardini, M. Tello, V. Cazcarra-Bes, K. Papathanassiou and I. Hajnsek, "L-and P-band 3-D SAR reflectivity profiles versus lidar waveforms: The AfriSAR case.," *IEEE Journal of Selected Topics in Applied Earth Observations and Remote Sensing,* vol. 1, 2018.

[45] M. Pardini, V. Cazcarra-Bes and K. P. Papathanassiou, "TomoSAR Mapping of 3D Forest Structure: Contributions of L-Band Configurations," *Remote Sensing,* vol. 13, no. 12, p. 2255, 2021.

[46] R. Guliaev, M. Pardini and K. P. Papathanassiou, "A Comparison of Function Bases for Polarization Coherence Tomography in Forest Scenarios," in *13th European Conference on Synthetic Aperture Radar. VDE*, 2021.

[47] S. Cloude, "Polarization coherence tomography," *Radio Science ,* vol. 41, no. 4, pp. 1-27, 2006.

[48] E. Aguilera, M. Nannini and A. Reigber, ""Wavelet-Based Compressed Sensing for SAR Tomography of Forested Areas," *IEEE Transactions on Geoscience and Remote Sensing,* vol. 51, no. 12, pp. 5283-5295, 2013.